Journal of Catalysis 432 (2024) 115435

Contents lists available at ScienceDirect

Journal of Catalysis

journal homepage: www.elsevier.com/locate/jcat

Kinetics and reaction mechanism of Pd-Catalyzed chlorobenzene hydrogenolysis

Nikki Kragt [a,1], Jalal Tavana [b,1], Mohammed Al-Gharrawi [b], M. Clayton Wheeler [b], David Hibbitts [a,*], Thomas J. Schwartz [b,*]

[a] Department of Chemical Engineering, University of Florida, Gainesville, FL 32611, USA
[b] Department of Chemical and Biomedical Engineering, University of Maine, Orono, ME 04469, USA

ARTICLE INFO

Keywords:
Hydrogenolysis
Reaction Kinetics
Density Functional Theory
Reaction Mechanisms
Environmental Remediation

ABSTRACT

Chlorinated organic compounds are ubiquitous chemical intermediates, final products, and waste streams found in multiple industries. These compounds must often be dechlorinated prior to disposal to avoid negative consequences for environmental and human health. In this work, we employ kinetic experiments and density functional theory (DFT) to examine Pd-catalyzed chlorobenzene hydrogenolysis, which is highly selective for the formation of benzene (>95 %). Kinetic data (353 K, 10–101 kPa H_2, 0.2–1.1 kPa C_6H_2Cl, 0.5–1 kPa HCl) on 5 wt% Pd/C catalysts revealed rates that are first-order, half-order, and inverse first-order with respect to PhCl, H_2, and HCl, respectively. These kinetic trends are consistent with PhCl dechlorination as the kinetically relevant step occurring at a single site on surfaces saturated by Cl adatoms (Cl*) in equilibrium with H_2 and HCl, consistent with previous reports in the literature. However, the nature of this C−Cl bond activation has not been well-described in the prior literature, because forming adsorbed Ph* and Cl* typically requires two sites, yet the kinetic trends suggest that only a single site is needed. Here, we resolve this inconsistency using theory, which shows that Cl* saturates Pd surfaces at a Cl*:Pd_{surf} ratio of *ca.* 0.3–0.4. This low saturation coverage enables Ph* (and other species) to bind interstitially among the Cl* adatoms without requiring Cl* desorption. Theory furthermore confirms that the reaction occurs through a rate-determining PhCl dechlorination, without any C–H activation of the phenyl ring. This non-competitive binding of Ph* among Cl* adatoms can be described as a two-site mechanism that agrees with the kinetic, isotopic, and theoretical data from this and prior work.

1. Introduction

Chlorinated organic compounds (COCs) are important chemical solvents and precursors used to produce materials such as dyes, pesticides, petrochemicals, and pharmaceuticals.[1–3] Processes involving these compounds also generate waste streams containing COCs. Both the use of chlorinated products and the generation of chlorinated industrial wastes introduce COCs into the environment, where they become persistent organic pollutants due to their toxicity, carcinogenicity, and thermal stability.[1,4,5] For decades, society has recognized the danger of COCs on both environmental and human health and has employed numerous methods for waste stream and water treatment to address this public health concern.[2,6,7] Incineration is often the most economical option owing to lower energy demands; however, it can lead to the net production of polychlorinated species, which are sometimes more toxic than the chlorinated starting materials.[5,8–10] Advanced oxidation technologies, such as photocatalysis and ozonation, have proven effective for polluted water treatment, but are less practical for other applications because of high energy consumption.[10,11] Adsorption processes also prove costly given the materials required,[2,12] while biological treatment generally occurs at relatively low conversions.[9,10] Every method developed to date has drawbacks, and treatment facilities still need a method that is efficient, effective, and can keep pace with increasingly stringent regulations enforced under the Clean Water and Clean Air Acts.[6,8]

Catalytic hydrodechlorination, whereby Cl is removed from organic species via C−Cl hydrogenolysis, is a low-energy alternative. It transforms pollutants to valuable raw materials while producing little to no CO_2, NO_x, or additional toxic emissions,[3,5,10,13,14] making it one of the preferred methods of dechlorination in comparison to other methods

* Corresponding authors.
E-mail addresses: hibbitts@ufl.edu (D. Hibbitts), thomas.schwartz@maine.edu (T.J. Schwartz).
[1] These authors contributed equally

https://doi.org/10.1016/j.jcat.2024.115435
Received 15 December 2023; Received in revised form 6 March 2024; Accepted 9 March 2024
Available online 11 March 2024

of processing.[9] Given its abundant advantages, C−Cl hydrogenolysis is an important process option for environmental remediation of contaminated water and industrial waste. Unfortunately, catalyst deactivation, generally by strongly bound chlorine adatoms, is frequently encountered in C−Cl hydrogenolysis.[5,15,16] Catalyst deactivation during C−Cl hydrogenolysis can be reversible or irreversible depending on the identity of the catalyst used and the nature of the poison.[17] Consequently, it is worthwhile to continue studying this process because understanding C−Cl hydrogenolysis mechanisms of various organic wastes can help us learn to prevent catalyst deactivation, improve reaction selectivity, and improve the overall process.

Hydrogenolysis reactions, more broadly, have been extensively studied, and classes of reactions share similar mechanistic attributes. Comprehensive studies of metal-catalyzed hydrogenolysis of saturated carbon–carbon bonds have established that C–C hydrogenolysis occurs by first cleaving C–H bonds to form a hydrogen-deficient adsorbed intermediate followed by C–C cleavage, which is the rate-determining step.[18–34] One study examining gas-phase C−Cl hydrogenolysis of saturated chlorofluoroethanes (CF_3CFCl_2, CF_3CF_2Cl, CF_3CCl_3, and CF_3CFClH) on Pd catalysts concluded the reaction is first-order, half-order, and inverse first-order with respect to the chlorinated reactant, H_2, and HCl, respectively.[35] The authors proposed a mechanism in which C−Cl bond cleavage is the rate-determining step and the chlorofluoroethane reactants adsorb to a single site before transition state formation.[35] However, the proposed hydrogenolysis mechanism was an approximation; the single-site adsorption complex was proposed solely because it sufficiently described the kinetics data, as possible unsaturated intermediates on the surface were unknown.[35] Additionally, the apparent activation energies for each reaction varied over the range from 80 to 145 kJ mol^{-1}, where relative activation energy differences among reactants did not match relative differences in bond energies, indicating the actual mechanisms by which C−Cl hydrogenolysis occurred were possibly different for each reactant.[35] A later periodic density functional theory (DFT) study including C−Cl bond cleavage in methyl chloride predicted that C−Cl cleavage follows the removal of two hydrogens from the carbon atom to form a *HCCl* intermediate on groups 9–10 transition metals,[27] but compounds with more halogens or other functional groups have not been similarly examined. It is widely accepted that Pd-containing catalysts are preferred for dechlorination [2,9,13,16,36–39] as they exhibit superior efficiency and stability in comparison to other catalysts tested, which has been demonstrated for a variety of chlorinated species, including chlorophenol[4] and 4-chloro-2-methylphenoxyacetic acid.[36]

As chlorinated organic wastes are often aromatic species, chlorobenzene (PhCl) is a preferred model compound for conducting fundamental studies of C−Cl hydrogenolysis for remediation purposes.[40] Hydrogenolysis reactions involving aromatic species have also been extensively studied, often to selectively cleave carbon-heteroatom bonds and preserve the arene through the course of the reaction. These prior studies have indicated a competition between hydrogenolysis and hydrogenation of the aromatic ring.[4,41–45] Palladium catalysts are preferred for PhCl hydrogenolysis, as they are highly reactive and known to produce mostly benzene with negligible excess hydrogenation to cyclohexane[46] but are still subject to inhibition by HCl.[47] A study on gas-phase PhCl hydrogenolysis at 353 K found Cl* inhibited reaction rates of PhCl hydrogenolysis by the same order of magnitude on Pd/Al_2O_3 and Rh/Al_2O_3 catalysts, despite the 100 times greater reactivity of Pd/Al_2O_3.[47] Measured reaction orders for PhCl, H_2, and HCl were 1, 0.5, and −1, respectively (353 K, 0.06–8.5 kPa PhCl, 0.02–0.4 Torr HCl, 1.7–101 kPa H_2).[47] The reaction order with respect to PhCl decreased to zero as PhCl pressure increased, including at pressures of PhCl that cause its condensation.[47] The reaction scheme proposed in that study to describe the observed kinetic behavior of PhCl hydrogenolysis is the currently prevailing reaction scheme accepted and referenced (Eq. (1)–(3)).[47]

$$C_6H_5Cl(g) + H^* \underset{k_1}{\rightarrow} Cl^* + C_6H_6(g) \quad (1)$$

$$HCl(g) + H^* \underset{k_2}{\rightarrow} H_2(g) + Cl^* \quad (2)$$

$$H_2(g) + Cl^* \underset{k_H}{\rightarrow} HCl(g) + H^* \quad (3)$$

This mechanism, however, implies an Eley-Rideal style dechlorination in which an unbound PhCl reacts with a bound H* in a single elementary step to form Cl* and an unbound benzene—a pathway that challenges our intuitions of surface chemistry. Assuming equal rates of surface reduction and chlorination and that the surface is entirely covered with adsorbed H* and Cl*, the corresponding rate equation describes a reaction where chlorobenzene and HCl interact with the surface to form Cl*, PhCl and HCl compete for adsorption, and hydrogen cleans the surface (Eq. (4)).[47]

$$r = \frac{k_1 k_H P_{C_6H_5Cl} P_{H_2}^{0.5}}{k_1 P_{C_6H_5Cl} + k_2 P_{HCl} + k_H P_{H_2}^{0.5}} \quad (4)$$

Batch-style liquid-phase experiments on the reactivity of PhCl and *para*-substituted PhCls (amino-, methoxy-, methyl-, chloro-, acetyl- and cyano-PhCl) over Pd/C catalysts in hexadecane found that the reaction is accelerated by both electron-donating and electron-withdrawing substituents.[48] Measured reaction orders for all reactants examined ranged from 0.91 to 0.99 [573 K, (1.2–3.6) × 10^{-3} mol chlorinated reactant, 1 MPa H_2].[48] The same study found reaction orders with respect to non-substituted PhCl and H_2 to be approximately 0.9 and 0.52, respectively.[48] The kinetic behavior of HCl was not examined.

Most previous studies interpreted solely experimental data or focused on catalyst synthesis and characterization, so despite the extensive knowledge gained from previous studies of PhCl hydrogenolysis on Pd, the mechanism behind measured kinetic behavior is poorly understood. This work aims to couple gas-phase kinetics experiments and contemporary DFT methods to elucidate the state of the catalyst surface and understand the mechanism of PhCl hydrogenolysis without added complications, such as the presence of a liquid. PhCl hydrogenolysis is performed on 14 nm 5 % Pd/C catalyst particles at 353 K, to allow direct comparison with prior work,[47] as well as temperatures of 313 K, 323 K, and 343 K to evaluate temperature effects on reaction kinetics. Catalyst stability was examined and compared to that observed in previous literature. Kinetics experiments were conducted at partial pressures ranging from 10−101 kPa H_2, 0.2–1.1 kPa PhCl, and 0.5–1.0 kPa HCl, at 50 % PhCl conversion. Kinetic isotope experiments were also performed with 99.6 kPa D_2, and mass transfer limitations were evaluated before data analysis and development of a proposed mechanism. DFT-derived electronic, enthalpic, entropic, and free energy activation barriers were used to supplement mechanism development and concurrently explain observed experimental behavior.

2. Methods

2.1. Experimental methods

2.1.1. Catalyst Preparation

A 5 wt% palladium catalyst was prepared by incipient wetness impregnation with an aqueous solution of $Pd_2(NO_3)\cdot xH_2O$ (Strem Chemicals, 99.9 %) onto a carbon black support (Cabot Corporation, Vulcan XC-72). The Vulcan XC-72 support used here was chosen for its inertness and lack of S and N impurities that may influence the reaction kinetics. The catalyst was dried overnight at 383 K, after which it was reduced directly in a 50 sccm stream of flowing dihydrogen (Matheson, 99.999 %) for 4 h at 533 K (10 K min^{-1}). The catalyst was passivated for 12 h at room temperature in a dilute mixture of air and argon.

2.1.2. Catalyst Characterization

CO chemisorption measurements were performed using a Micromeritics ASAP 2020 instrument. The passivated catalysts were placed in a quartz sample tube between two layers of quartz wool, after which the sample was evacuated and re-reduced at 673 K in flowing dihydrogen for 2 hr. Adsorbed hydrogen atoms were removed by desorption under vacuum (10^{-5} torr dynamic vacuum) at 673 K for 1 hr. CO chemisorption was performed at 308 K using CO equilibrium pressures ranging between 0.5 and 313 torr. Pd dispersion and the average Pd nanoparticle size were obtained from the CO saturation coverage assuming a CO/Pd_{surf} stoichiometry of 2:3[49] and a relationship between dispersion, D, and particle size, d, of $d = \frac{1.1}{D}$. [50] Mean particle diameter was estimated to be 14 nm from the irreversible uptake of CO at 308 K (Fig. S1). If a 1:1 stoichiometry was used instead, the particle size would be 21 nm, so the mean particle diameter can be stated as in the range of 14–21 nm with reasonable confidence.

2.1.3. Reaction Kinetics Measurements

Reactions were carried out at ambient pressure in a glass stirred-tank reactor (Chemglass Model CG-1949-X-303) configured to operate in continuous mode, with the feed stream being preheated to reaction temperature. The reactor vessel was originally designed for liquid-phase reactions. To modify it for gas-phase reactions, the impellor blades were replaced with four homemade polyether ether ketone (PEEK) mesh baskets (mesh size = 50) affixed to the glass impellor shaft using a custom-machined Teflon bracket. These baskets are designed to receive the powder catalyst and spin it through the bulk vapor phase in a Carberry reactor configuration.[51] The Teflon anchor stirrer at the bottom of the impellor shaft was retained to facilitate additional mixing. All standard taper joints were greased with H-grease (Apiezon). A pressure relief valve (Chemglass Part No. CG-999–02) was set to 3 psig and used to prevent over-pressurization of the glass vessel. A pressure gauge (Ashcroft Part No.94575XLL) was affixed to a Teflon stopper and used to monitor the pressure in the reactor vessel. Heating was provided in the jacketed portion of the vessel using a circulating heating bath (Fisher Scientific, Isotemp Model 6200 H7) containing propylene glycol antifreeze purchased from a local hardware store. Heating was provided to the vessel head by a resistive heating tape (HTS/Amptek), and the whole vessel was wrapped in ceramic insulation. The reactor temperature was measured by a Hastelloy-sheathed K-type thermocouple (Omega, Inc.). Temperature control was provided by a combination of the circulating heating bath, which was set at the reaction temperature, and by the heating tape on the reactor head, via a PID temperature controller (SOLO 4848, Automation Direct) using input from the main reactor thermocouple. Measurement of the temperature at several points in the reactor vessel (achieved by moving the main reactor thermocouple) showed there to be no temperature gradients in the bulk vapor phase of the reactor.

For a typical reaction, 0.05 g of catalyst was diluted in 0.75 g of carbon black using an agate mortar and pestle. This diluted catalyst was loaded into the four PEEK mesh baskets on the reactor impellor shaft. The catalyst was reduced in flowing dihydrogen (60 sccm, 99.999 %, Matheson) at 353 K for 1 h, after which the reactor was set to the desired temperature. Liquid PhCl (>99 %, Acros Organics) was fed from a syringe pump (NE-1000, New Era Pump Systems) through a 1/8 in. outer diameter Teflon tube into a stream of flowing dihydrogen (99.999 %, Matheson) or dideuterium (99.99 %, 99.99 atom% D, Airgas) mixed with helium (99.999 %, Matheson). The dihydrogen and helium flow rates were controlled by calibrated metering valves (SS-SS2-VH, Swagelok). The liquid and gas flow rates were chosen to keep the partial pressure of PhCl in this gas stream below its vapor pressure at 298 K. The vapor feed was introduced to the reactor through a glass spiral tube condenser (Chemglass Part No. CG-1215-C-01) used to pre-heat the feed. Periodically, the reactor was checked for inertness by feeding a mixture of PhCl and dihydrogen at the reaction temperature to the reactor vessel in the absence of a catalyst; no conversion of PhCl was observed during these runs. The effect of HCl on the reaction rate was probed by co-feeding HCl gas (1000 ppm in He, Research Grade, Airgas), delivered through a 1/8 in. outer diameter Teflon line to the reactor vessel.

The reaction products were quantified using a gas chromatograph equipped with a flame ionization detector (GC-FID, MG-5, SRI Instruments) and a capillary column (MXT-1, Restek). Reaction rates were measured at four different temperatures (313 K, 323 K, 343 K, and 353 K) and a variety of partial pressures of PhCl, dihydrogen, and HCl, controlled by varying the flowrates of each species and the flowrate of the He diluent. Turnover frequencies (TOFs) were obtained by normalizing the reaction rates, r, to the CO uptake, n_{CO}, as shown in Equation (5). Selectivities were calculated according to Equation (6), where F_i corresponds to the molar flow rate of species i leaving the reactor.

$$\mathrm{TOF}\left(\mathrm{s}^{-1}\right) = \frac{r(\mu\mathrm{mol\ g}^{-1}\ \mathrm{s}^{-1})}{n_{CO}(\mu\mathrm{mol\ g}^{-1})} \tag{5}$$

$$\mathrm{Selectivity}_i = \frac{F_{\mathrm{prod,i}}}{\sum_i F_{\mathrm{prod,i}}} \times 100\% \tag{6}$$

2.2. Computational methods

Periodic density functional theory (DFT) calculations were performed using the Vienna ab initio simulation package[52–56] in the computational catalysis interface (CCI).[57] Almost all calculations used the revised Perdew-Burke-Ernzerhof (RPBE) form of the generalized gradient approximation (GGA) to describe exchange–correlation energies; select calculations used the Perdew-Burke-Ernzerhof (PBE) functional, and such calculations are labeled accordingly.[58–60] Similarly, select calculations used the DFT-D3[61,62] method to calculate dispersive interaction energies, which are absent in the RPBE and PBE functionals. To describe core-valence interactions, plane waves were assembled using the projector augmented-wave (PAW) method with an energy cutoff of 396 eV.[63,64]

Gas-phase molecules were modeled in a vacuum space of 18 Å × 18 Å × 18 Å. The catalyst was modeled as a flat 4 × 4 Pd(1 1 1) periodic lattice consisting of four layers in the z-direction with 10 Å of vacuum space above the slab. The top two metal layers were allowed to relax and the bottom two metal layers were fixed in position. Gas-phase and flat surface structures were optimized using a three-step process involving two geometric convergence steps followed by a single-point calculation to determine energy minima. This process is available in CCI and increases CPU efficiency over traditional single-step calculations.[57] Forces on all atoms were calculated using a fast Fourier transform (FFT) grid and were constrained by a maximum threshold of 0.05 eV $Å^{-1}$. Wavefunctions were converged until electronic energies varied by less than 10^{-4} eV using an FFT grid 1.5× the plane wave cutoff in the first and third steps, and by less than 10^{-6} eV using an FFT grid 2× the plane wave cutoff in the second step calculation. Gas-phase calculations sampled the Brillouin zone at the Γ-point in all steps. Optimizations of the bare catalyst surface used a 4 × 4 × 1 Monkhorst-pack sampling of the first Brillouin zone (k-point mesh)[65,66] for the first two steps and an 8 × 8 × 1 k-point mesh in the third step.

The nudged elastic band (NEB)[67,68] and dimer[69] methods were used in combination to isolate transition state structures. The NEB method was performed using 16 images and converged to a force of <0.3 eV $Å^{-1}$. Wavefunctions were converged to less than 10^{-4} eV using a 3 × 3 × 1 k-point mesh and an FFT grid 1.5× the plane wave cutoff. The dimer method was used to optimize transition state structures with the three-step calculation process available in CCI as described above, excepting a 3 × 3 × 1 k-point mesh which was used for the first two steps and a 6 × 6 × 1 k-point mesh which was used in the third step. Reactant and product structures were optimized similarly. Vibrational frequency calculations were used to calculate zero-point energies and thermal corrections to estimate enthalpies (H), entropies (S), and free energies

(G) of reactants, products, and transition states at 353 K. Frequency calculations also confirm the presence of a single imaginary frequency and associated reaction mode for transition states. For gas species, translational and rotational partition functions were included in free energy calculations, as described in further details in the SI (Section S7).

For our analysis, we assume that C−Cl bond cleavage is the rate-determining step and that adsorption, desorption, and dehydrogenation steps are quasi-equilibrated. These assumptions are supported by numerous experimental[18,20,22,25,70–72] and computational [18–21,23,27,71] studies conducted prior to this work. The effective enthalpy barrier ($\Delta H^{\ddagger}$; Eq. (7)) is consequently defined as the enthalpy difference between the transition state ($C_6H_{5-y}Cl^{\ddagger}$) and the Cl*-covered surface with stoichiometric amounts of gas-phase HCl, H_2, and PhCl:

$$\Delta H^{\ddagger} = H\left[C_6H_{5-y}Cl^{\ell^*,\ddagger}\right] + \ell H[HCl(g)] - \frac{\ell - y}{2}H[H_2(g)] - H[C_6H_5Cl(g)] - H[\ell Cl^*] \quad (7)$$

with ℓ representing the number of Cl* that desorb from the Cl*-covered surface (in equilibrium with H_2 and HCl) and y representing the number of hydrogens removed from the phenyl ring prior to transition state formation. The effective entropy barrier ($\Delta S^{\ddagger}$; Eq. (8)) is similarly defined:

$$\Delta S^{\ddagger} = S\left[C_6H_{5-y}Cl^{\ell^*,\ddagger}\right] + \ell S[HCl(g)] - \frac{\ell - y}{2}S[H_2(g)] - S[C_6H_5Cl(g)] - S[\ell Cl^*] \quad (8)$$

These values can be used to calculate the effective free energy barriers ($\Delta G^{\ddagger}$; Eq. (9)):

$$\Delta G^{\ddagger} = \Delta H^{\ddagger} - T\Delta S^{\ddagger} \quad (9)$$

which can be used to calculate effective reaction rate constants.

3. Results and discussion

3.1. Kinetic measurements

The impacts of external and internal mass transfer were evaluated to confirm reaction rates would be measured at reaction-limited conditions. TOFs were measured while increasing stirring speed to decrease boundary layer thickness in gas-phase batch reactions (353 K, 101 kPa H_2, 0.2 kPa PhCl). TOFs vary little at stirring speeds above 300 rpm (Fig. S2), identifying that operation with stirring speeds above 300 rpm minimizes external mass transfer limitations. The Weisz-Prater criterion, which rules out significant internal mass transfer limitations if it is much less than 1 (Eq. S1), was calculated to be 0.047 at these conditions [73]. This leads to a corresponding effectiveness factor (η; Eq. S2) of 0.98 [74]. The absence of significant external and internal mass transfer limitations confirms that reaction rates are measured at reaction-limited conditions for stirring speeds greater than 300 rpm.

The reaction consistently demonstrates >95 % product selectivity toward benzene over cyclohexane at 353 K, 97 kPa H_2, 1.1 kPa PhCl (Fig. 1); therefore, only benzene production rates will be used in subsequent kinetic analyses. High selectivity toward benzene is consistent with results in other PhCl HDC studies using Pd-containing catalysts. [9,15,16,37,39,46,48] Minimal variation was observed in TOFs of PhCl consumption, benzene production, and cyclohexane production over 50 h, demonstrating stability of the catalyst for at least 50 h on stream. This indicates that deactivation or irreversible poisoning of the catalyst via chlorination or any other mechanism is not an observable issue at these conditions (H_2:PhCl ratio > 1).

Measured hydrogenolysis TOFs on 5 wt% Pd/C particles at varying pressures of PhCl, H_2, and HCl are shown in Fig. 2 (313–353 K). Rates increase with increasing PhCl pressure at high temperature (353 K) and are nearly insensitive to PhCl pressure at low temperature (313 K), with predicted reaction orders shifting from +0.8 to −0.3 (uncertainties shown in Table S1 of the SI). This suggests that as temperatures

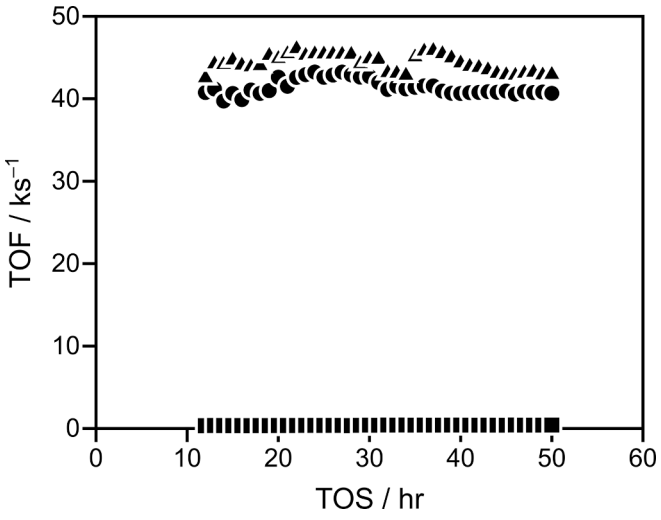

Fig. 1. Hydrogenolysis TOFs of PhCl (▲), benzene (●), and cyclohexane (■) as a function of time on stream (TOS) measured on 14 nm 5 % Pd/C particles at 353 K, 97 kPa H_2, 1.1 kPa PhCl, and 50 % PhCl conversion.

decrease, PhCl becomes an abundant surface-bound species, leading to an expected zero-order kinetic behavior. Rates always increase with H_2 pressure (313–353 K) and the H_2 reaction order is nearly independent of temperature; it increases from 0.3 to 0.6 as temperature increases. HCl decreases rates as expected because it will increase the coverage of site-blocking Cl* species and the reaction order is close to −1, despite a large scatter and a large uncertainty (Table S1). Although the effect of temperature on HCl pressure dependence was not measured, we expect little-to-no variation in the reaction order with respect to HCl as temperature changes; because Cl* only desorbs as HCl during this reaction, hydrogen pressure dependence is a proxy for HCl pressure dependence and varies only slightly across this temperature range. These reaction orders for PhCl, H_2, and HCl are consistent with those reported in previous works.[35,47,48] In particular, prior studies[35,47,48] also saw HCl reaction orders near −1, giving extra confidence to that interpretation despite the large scatter in the present data.

The reaction orders for PhCl, H_2, and HCl measured at 353 K are consistent with the underlying assumptions of Sinfelt's mechanism for C−Cl hydrogenolysis (shown in Scheme S1),[18] where adsorption, desorption, and hydrogenation/dehydrogenation steps are assumed to be quasi-equilibrated and C−Cl bond activation is assumed to be rate-determining. Quasi-equilibrium assumptions are supported here by kinetic isotope effect (KIE) experiments, which found no significant difference between TOFs for the reaction involving both H_2 and D_2 as reactants (rate ratio of D_2/H_2 = 1.03; Fig. S3). From this result, it is evident that hydrogen (molecular or dissociated) is not involved in the rate-determining step, signifying that any reaction steps involving H_2 dissociation, hydrogenation of Cl*, possible dehydrogenation of PhCl, or hydrogenation of Ph* to form benzene are kinetically insignificant.

As discussed in Section S5 of the SI, no rate equation that assumes both that C−Cl bond activation is rate-determining and that all surface species (*e.g.*, Ph*, Cl*) compete for equivalent sites can explain the experimental behavior of TOFs as a function of PhCl, H_2, and HCl pressures shown in Fig. 2 (or comparable experiments reported in the literature[35,47,48]). However, if Cl* does not compete for adsorption sites with PhCl*, Ph*, or H* (*i.e.*, adsorption of PhCl* does not require desorption of a Cl* from the Cl-covered surface), then the mechanism proposed by Sinfelt can be used to explain our kinetic trends. Such non-competition is shown in Scheme 1, which describes a mechanism that invokes two unique sites, denoted $*^a$, which binds Cl*, and $*^b$, which binds PhCl*, Ph*, and H*. Scheme 1 is consistent with our experimental observations and retains the key assumptions that underly Sinfelt's proposed mechanism[18] for hydrodechlorination reactions, *i.e.*, that

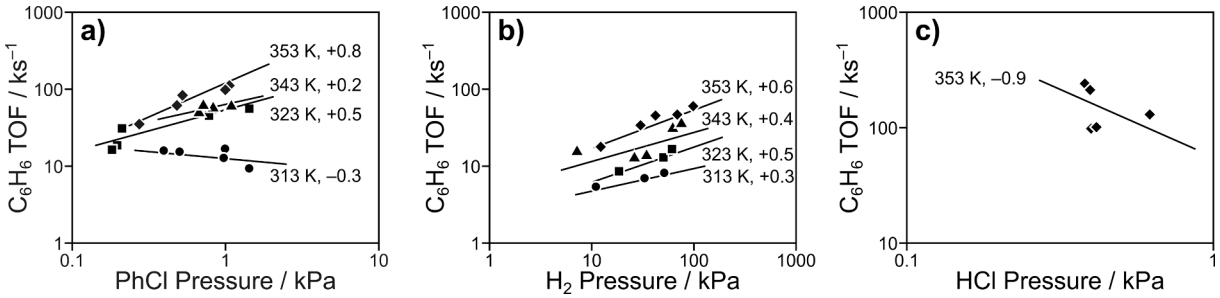

Fig. 2. Hydrogenolysis TOFs on 14 nm 5 wt% Pd/C particles and 50 % PhCl conversion at temperatures of 313 K (●), 323 K (■), 343 K (▲) and 353 K (◆). Plots show effects of (a) PhCl pressure at 97 kPa H_2, (b) H_2 pressure at 1 kPa PhCl, and (c) HCl pressure at 97 kPa H_2 and 1 kPa PhCl. Lines are to guide the eye. Reaction temperatures are followed by corresponding calculated reaction orders.

$$H_2\,(g) + 2{*^b} \underset{K_1}{\rightleftharpoons} 2H{*^b} \qquad 1.1$$

$$HCl\,(g) + {*^a} + {*^b} \underset{K_2}{\rightleftharpoons} H{*^b} + Cl{*^a} \qquad 1.2$$

$$C_6H_5Cl\,(g) + {*^b} \underset{K_3}{\rightleftharpoons} C_6H_5Cl{*^b} \qquad 1.3$$

$$C_6H_5Cl{*^b} + {*^a} \xrightarrow[k_4]{} C_6H_5{*^b} + Cl{*^a} \qquad 1.4$$

$$C_6H_5{*^b} + H{*^b} \underset{K_5}{\rightleftharpoons} C_6H_6{*^b} + {*^b} \qquad 1.5$$

$$C_6H_6\,(g) + {*^b} \underset{K_6}{\rightleftharpoons} C_6H_6{*^b} \qquad 1.6$$

Scheme 1. Proposed two-site mechanism and intermediates in PhCl hydrogenolysis on 5% Pd/C particles. ($*^a$ denotes surface sites occupied by species that require Cl* to desorb and $*^b$ denotes surface sites occupied by species that do not require Cl* to desorb).

adsorption, desorption, and dehydrogenation steps are quasi-equilibrated and C−Cl bond activation is rate-determining. We further justify the assumption that PhCl* and Cl* bind non-competitively using DFT calculations of PhCl dissociations, and Cl*, PhCl*, and H* adsorptions at varying Cl* coverages (*vide infra*).

Quasi-equilibrated hydrogen dissociation (Step 1.1) facilitates Cl* desorption from the catalyst surface in the form of HCl (Step 1.2). PhCl adsorption (Step 1.3) and benzene desorption (Step 1.6) are also assumed to be quasi-equilibrated. Adsorbed PhCl undergoes an irreversible C−Cl activation (Step 1.4) to produce C_6H_5* and Cl*. The C_6H_5* intermediate and H* combine to produce adsorbed benzene via a quasi-equilibrated C–H bond formation (Step 1.5). We chose to use a two-site mechanism not to indicate distinct sites present on the catalyst, but instead to emphasize that PhCl* and Cl* do not compete for sites (as discussed above) and that an adsorbed phenyl can be accommodated on the surface (at a site denoted $*^b$) without concomitant desorption of Cl* (from sites denoted $*^a$, discussed further in Section 3.2). This mechanism also assumes H* adsorbs without requiring desorption of Cl* due to its small size and that C_6H_6*, C_6H_5*, and H* are not abundant surface intermediates. These elementary steps and associated assumptions can be used to derive a rate equation:

$$\frac{r}{[L]} = \frac{k_4 K_3 P_{PhCl}}{\left(\frac{K_2 P_{HCl}}{K_1^{0.5} P_{H_2}^{0.5}}\right)(1 + K_3 P_{PhCl})} \qquad (11)$$

that describes dechlorination rates and the effects of PhCl, HCl, and H_2 pressures shown above. The denominator of Eq. (11) contains site-blocking terms that imply that Cl* is the sole MASI of the '*a*'-sites (*i.e.*, Cl* competes with Cl* for surface sites) and PhCl* is a possible '*b*'-site MASI. At high PhCl* coverages, rates will become zero-order in PhCl pressure by Eq. (11), consistent with the decrease in PhCl reaction orders with decreasing temperature. However, at all conditions of interest the reaction order in HCl is −1 and in H_2 is +0.5, suggesting that the surface remains saturated in Cl*.

Based on the site and reversibility assumptions described in Scheme 1 and transition state theory, the reaction can be described as:

$$C_6H_5Cl(g) + \ell Cl^* + 0.5\ell H_2(g) \underset{\Delta G^\ddagger}{\rightarrow} [C_6H_5 - Cl^\ddagger]^{\ell *} + \ell HCl(g) \qquad (12)$$

when occurring at low PhCl coverages, where ℓ represents the number of Cl* that must desorb (in the form of HCl, by reduction with 0.5ℓ H_2) from the surface to allow for transition state formation; in other words, it represents the number of 'a' sites required for this reaction. Other hydrogenolysis reactions (*e.g.*, of alkanes, oxygenates, etc.) occur after the dehydrogenation of involved C atoms to form C−M bonds that weaken the bond undergoing hydrogenolysis. Mechanisms involving partial or complete dehydrogenation of C atoms in C−X bond hydrogenolysis have been demonstrated for alkane hydrogenolysis, alkanol hydrogenolysis, alkanethiol hydrogenolysis, and chloroalkane hydrogenolysis.[18,20,22,23,28–30,35,75–77] Therefore, a generalized reaction mechanism that includes the possibility of dehydrogenation of the phenyl ring was also considered and can be found in the SI (Scheme S2). The effective free energy barrier is still represented as the free energy change between the Cl* MASI and the PhCl transition state, but takes a slightly different form that incorporates the evolution of hydrogen from possible dehydrogenation of the phenyl ring:

$$C_6H_5Cl(g) + \ell Cl^* + 0.5\ell H_2(g) \underset{\Delta G^\ddagger}{\rightarrow} C_6H_{5-y}Cl^\ddagger + \ell HCl(g) + 0.5yH_2(g) \qquad (13)$$

where y reflects the degree of dehydrogenation of the aromatic ring, and ℓ reflects the site requirements of the reaction. The corresponding generalized rate equation takes the following form, for conditions of low PhCl coverage, and high Cl* coverage, where K_{DH} represents the sum of equilibrium constants for any C–H activations that occur before kinetically relevant C−Cl activation:

$$\frac{r}{[L]} = \frac{k_4 K_{DH} P_{PhCl}}{P_{H_2}^{0.5y}} \left(\frac{K_1^{0.5} P_{H_2}^{0.5}}{K_2 P_{HCl}}\right)^{\ell} \qquad (14)$$

Notably, the rate equation in Eq. (11) is consistent with Eq. (14) given $\ell = 1$ and $y = 0$. However, we also consider other possibilities, described below, to rule out by theoretical techniques. We also note that Eq. (14), and the analysis below, presumes the reaction occurs at temperatures high enough to avoid saturation of '*b*' sites with PhCl; such inhibition does not impact C−Cl activation and can be accommodated by including a $(1 + K_3 P_{PhCl})^{-1}$ term in Eq. (14) for reactions at low temperatures.

3.2. Theoretical assessments of dechlorination mechanisms and Cl* coverage effects

PhCl dechlorination was modeled on Pd(1 1 1) surfaces with a fully saturated phenyl ring and PhCl-derived adsorbates that had undergone all possible combinations of dehydrogenation events. The (1 1 1) surface facet was chosen to represent the catalyst surface, as this is the most stable facet and, thus, the most abundant surface facet by area present on larger catalyst particles, such as the 14 nm particles used in this work. The surface of the catalyst is known to be covered with Cl* at some amount, set by the equilibrium between the surface and H_2 and HCl (Steps 1.1 and 1.2 in Scheme 1). However, the reactions were first modeled on a bare 4 × 4 Pd(1 1 1) surface, thus ignoring the effects of Cl* coverage, to identify reasonable hydrogenolysis pathways.

Free energy activation barriers ($\Delta G^{\ddagger}$; Eq. (9)) for C−Cl cleavage over bare Pd(1 1 1) increase as the ring is dehydrogenated (Fig. 3). The $\Delta G^{\ddagger}$ values (353 K) for PhCl activation without dehydrogenation (146 kJ mol^{-1}) and with one dehydrogenated carbon vicinal to the chlorine leaving group (165 kJ mol^{-1}, hereafter denoted as *ortho*-$C_6H_4Cl^*$ to signify the position of the H-loss relative to the Cl substituent) are >100 kJ mol^{-1} lower than the $\Delta G^{\ddagger}$ values for all other considered pathways. These results suggest that very little, if any, dehydrogenation of PhCl occurs before dechlorination, in contrast to prior work examining alkanes and substituted alkanes (*e.g.*, CH_3Cl). This is likely because PhCl, unlike substituted alkanes, starts unsaturated and thus the C atom in the C−Cl bond of interest can bind to the surface without preceding dehydrogenation reactions. Because of the large differences in $\Delta G^{\ddagger}$, we only focused on PhCl* and *ortho*-$C_6H_4Cl^*$ activations when considering the added effect of Cl* coverage, which required estimating the operating coverage of Cl* atoms at these conditions.

The likely Cl* saturation of the reference state (θ_{sat}) was estimated for 3 × 3, 3 × 4, 3 × 6, and 4 × 4 Pd(1 1 1) surface models. For each surface, multiple unique configurations of Cl* binding sites at each coverage were considered, and we assumed Cl* was in equilibrium with H_2 and HCl for analysis purposes (Steps 1.1 and 1.2 in Scheme 1). The differential adsorption free energy of adding an additional Cl* to a surface containing *n* Cl* is defined as:

$$\Delta G_{diff} = G[(n+1)Cl^{*a}] - \left(G[nCl^{*a}] + G[HCl] - \frac{1}{2}G[H_2]\right) \quad (15)$$

Figure 4 shows ΔG_{diff} values to reach the most stable Cl* surface configurations at each coverage investigated. Calculated ΔG_{diff} become positive above coverages of 1/6 ML on the 3 × 6 and 3 × 4 surface models, 3/16 ML on the 4 × 4 surface model, and 1/9 ML on the 3 × 3

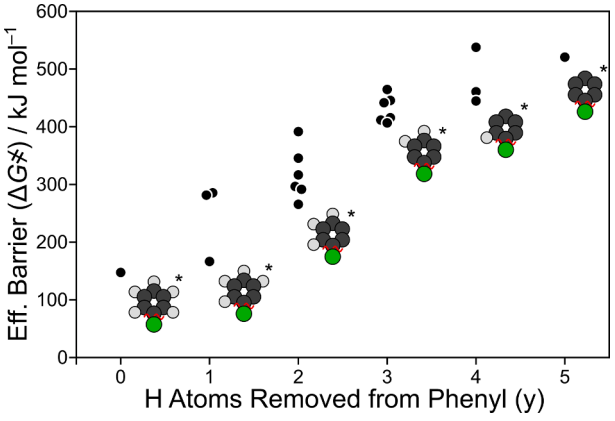

Fig. 3. Free energy barriers (ΔG≠; Eq. (9)) for C−Cl bond activation in PhCl-derived adsorbates on a bare 4 × 4 Pd(1 1 1) surface model (353 K, 1 bar H_2), where isomers corresponding to the lowest activation barrier at each saturation level are shown. Enthalpy barriers (ΔH≠; Eq. (7)) and tabulated data are shown in (Fig. S4, Table S4; SI).

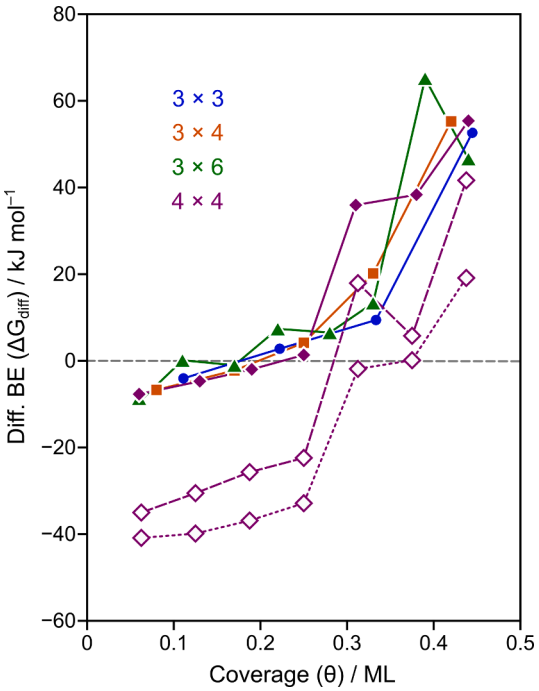

Fig. 4. Differential binding free energies (ΔG_{diff}; Eq. 16) for incrementally adding Cl* to lowest energy configurations on 3 × 3 (blue ●), 3 × 4 (orange ■), 3 × 6 (green ▲), and 4 × 4 (purple ◆) Pd(1 1 1) surface models (353 K). Calculations on the 4 × 4 surface model were also performed using the PBE functional (hollow purple ◆, dashed line) and the RPBE functional with the DFT-D3 method (hollow purple◆, dotted line). Differential binding enthalpies (ΔH_{diff}) and tabulated data are shown in the Supporting Information (Fig. S5, Table S5; SI).

surface model. Positive ΔG_{diff} values would be unlikely to result in adsorption at the given H_2:HCl ratios studied in this work (≥10), thus these points at which ΔG_{diff} becomes positive give a strong indication of the predicted coverage. However, the harmonic oscillator approximation used by DFT likely underestimates the entropy of the adsorbed Cl* species[78–82] and, therefore, overestimates the magnitude of the entropy loss upon adsorption (ΔS_{ads}). Furthermore, the exchange–correlation functional used here (RPBE) is likely to underpredict Cl* binding strength compared to others (*e.g.*, PBE, PW91).[58,83] Taken together, we suspect that our ΔG_{diff} are overestimated by DFT—that adsorption is expected to be more favorable than predicted. Given those factors, we estimate (using RPBE) that the saturation coverage of Cl* is 1/4 ML on 3 × 4 or 4 × 4 surfaces, or 1/3 ML on the Pd 3 × 3 or 3 × 6 surface models as those coverages coincided with large increases in ΔG_{diff}.

Indeed, ΔG_{diff} calculations done with PBE (for the 4 × 4 surface) led to values ~30 kJ mol^{-1} lower at low coverage (1/16 ML) than those obtained with RPBE, and about 10 kJ mol^{-1} lower at high coverage (7/16 ML). These PBE-derived ΔG_{diff} values also suggest a saturation coverage of 1/4 ML at the conditions (353 K, H_2:HCl > 10) of interest here. We also examined how dispersive interactions (estimated using the DFT-D3 method) influenced RPBE-derived ΔG_{diff} values. RPBE-D3 predicts ΔG_{diff} values similar to those predicted by PBE. This large shift is somewhat surprising given that Cl* adatoms would not be expected to have significant dipole–dipole interactions with a metal surface (in contrast to a species like hexane, where dispersive interactions are expected to dominate). Still, significant shifts in adsorption energy using dispersion-enabled methods (D3 or by using exchange–correlation functionals with van der Waals interactions built-in) have been seen for other small adsorbates such as CO*[84] and H*[23] in prior studies. RPBE-D3, like PBE and RPBE, suggests that Cl* saturates 4 × 4 surfaces near 0.25 ML.

These saturation coverages (0.25–0.33 ML, depending on the unit cell

size) match the maximum coverage for which Cl* can bind to three-fold sites without sharing metal atoms, which is dependent on the periodicity (and thus the unit cell size) of the surface model. At higher coverages, rather than share metal atoms, Cl* shifts to occupy bridge sites (Fig. 5e-f). Diffusion between the fcc and hcp binding modes (through the bridge site) has a barrier of only 9 kJ mol^{-1} at low coverage (1/16 ML), indicating the relative ease with which Cl* can reorganize to minimize repulsion between co-adsorbed species. The true coverage (*i.e.*, that not influenced by the symmetry requirements of these periodic surface calculations) is likely somewhere between 1/4 and 1/3 ML, but critically, all surface models investigated saturate with Cl* coverage well below a coverage of 1 ML.

The inability to reach a 1:1 Cl*:Pd$_{surf}$ stoichiometry is consistent with the measured Cl* saturation on Pd(1 1 1) at 300 K, θ_{sat} = 0.44 ML, determined from LEED studies of Cl* chemisorbed on single crystals. [85] That LEED study may have been able to reach 0.44 ML (above the 1/3 ML limit we predict) because of the lower temperature (300 K vs. 353 K here) or because Cl* is more willing to share surface metal atoms with coadsorbed Cl* or bind in bridge modes than our model predicts. If Cl* could bind in bridge sites without penalty, one would expect a maximum coverage of 0.5 ML without metal-atom-sharing among coadsorbed Cl*. These combined DFT and LEED data suggest that Cl* adsorbates are mobile on the Pd surface, repel one another, and prefer to bind in three-fold or bridge sites in a manner that results in adlayers with Pd atoms that are somewhat accessible to other adsorbates (*e.g.*, H*), as discussed below.

Dechlorination reactions of PhCl* (and *ortho*-C_6H_4Cl*) were modeled with a varying number of Cl* on the 4 × 4 Pd(1 1 1) surface; transition states are shown for PhCl* in Fig. 6. As Cl* coverage increases, the space occluded by the phenyl group decreases as it partially lifts off the surface (Fig. 6). This suggests that the phenyl group can alter its binding configuration to take up less space depending on the Cl* surface coverage. Since diffusion barriers for Cl* are relatively low and the Cl/Pd$_{surf}$ ratio is well below 1, Cl* can rearrange on the surface to accommodate additional adsorbed species. Thus, C_6H_5* can bind to the surface without requiring Cl* to desorb. The single-site requirement (ℓ = 1) suggested by the kinetics data (Section 3.1) reflects the need to desorb one surface Cl* to accommodate the additional adsorbed Cl* generated from C−Cl activation (the rate-determining step) and that one does not have to desorb an additional Cl* to accommodate the C_6H_5* product.

DFT calculations using RPBE or PBE, however, predict that 2Cl* are removed from the surface before PhCl dechlorination (Fig. 7). Effective free energy barrier ($\Delta G^{\ddagger}$; Eq. (9)) values for PhCl* dechlorination decrease from 161 kJ mol^{-1} to 148 kJ mol^{-1} (using RPBE) as the number of Cl* removed from the surface increases (ℓ) from 0 to 2, and then increase with additional Cl* removals. Using PBE, which predicts stronger binding of adsorbates (both Cl* and PhCl*), also sees that $\Delta G^{\ddagger}$ reaches a minimum value at an ℓ value of 2. Notably, PBE predicts lower $\Delta G^{\ddagger}$ values than RPBE at low ℓ values (0–1) and similar $\Delta G^{\ddagger}$ values at higher ℓ values (3–4). This behavior makes sense, as PBE predicts stronger binding than RPBE, and $\Delta G^{\ddagger}$ reflects a replacement of ℓ Cl* adatoms with a Ph−Cl* transition state, leading to a compensation effect that cancels out differences between the two functionals because the shifts in binding strength for Cl* and the Ph−Cl*‡ transition state are similar. However, comparing RPBE and RPBE-D3, the shifts in binding strength are dissimilar between Cl* and the Ph−Cl*‡ transition state because their sizes are so different. This results in RPBE-D3 predicting a smaller number of required vacancies—somewhere between 0 and 1—based on the very similar $\Delta G^{\ddagger}$ values (68 and 69 kJ mol^{-1}). It is likely that RPBE-D3 overestimates the adsorption energies of the PhCl-derived transition state (further discussed below), and that RPBE underestimates it, such that the true values are within the large ranges shown in Fig. 7. Barriers for C−Cl activation in *ortho*-C_6H_4Cl* continually decrease from 219 kJ mol^{-1} to 179 kJ mol^{-1} as the number of Cl* removed increases from 0 to 4 (using RPBE). These results, taken together, show that C−Cl activations in PhCl* are more likely than in partially dehydrogenated species (Figs. 3 and 7), and that, depending on the DFT methods used (RPBE, RPBE-D3, PBE), our model predicts that the reaction occurs after 0–2Cl* are removed (ℓ = 0–2) from the 0.25 ML Cl* resting state, capturing the measured value (of 1). This analysis of $\Delta G^{\ddagger}$ values, however, assumes that the C−Cl bond activation is the sole rate-determining step, which we can assess by examining the subsequent

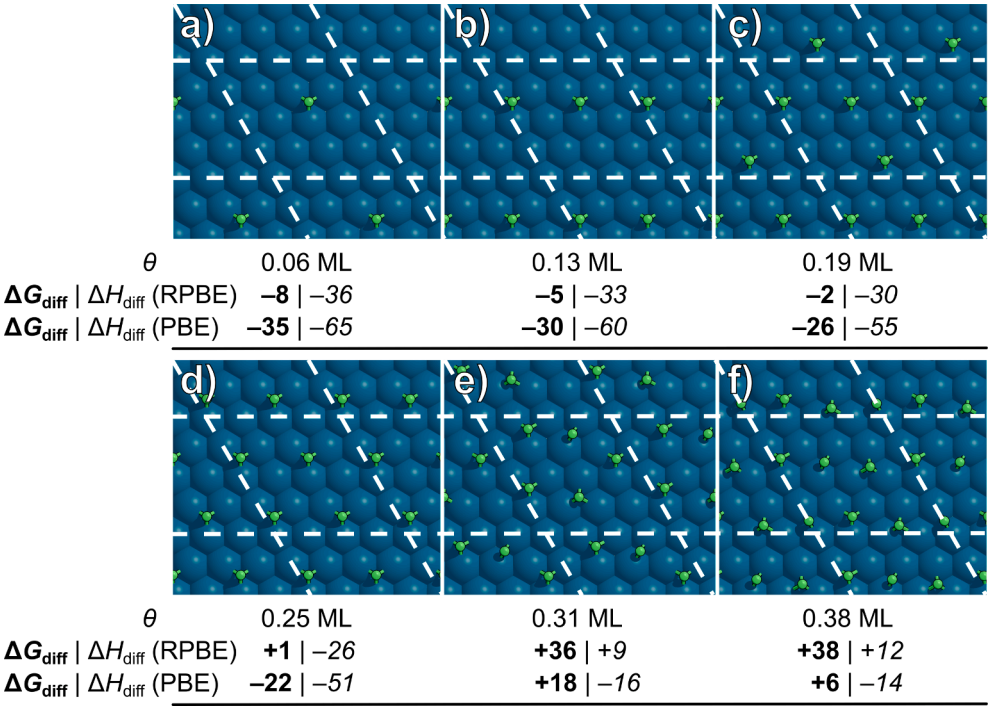

Fig. 5. Differential binding free energies (bold) and enthalpies (italic) in units of kJ mol^{-1} and corresponding Cl* surface configurations (a-f) for the 4 × 4 Pd(1 1 1) surface model at 353 K. The unit cell is denoted by the dashed lines.

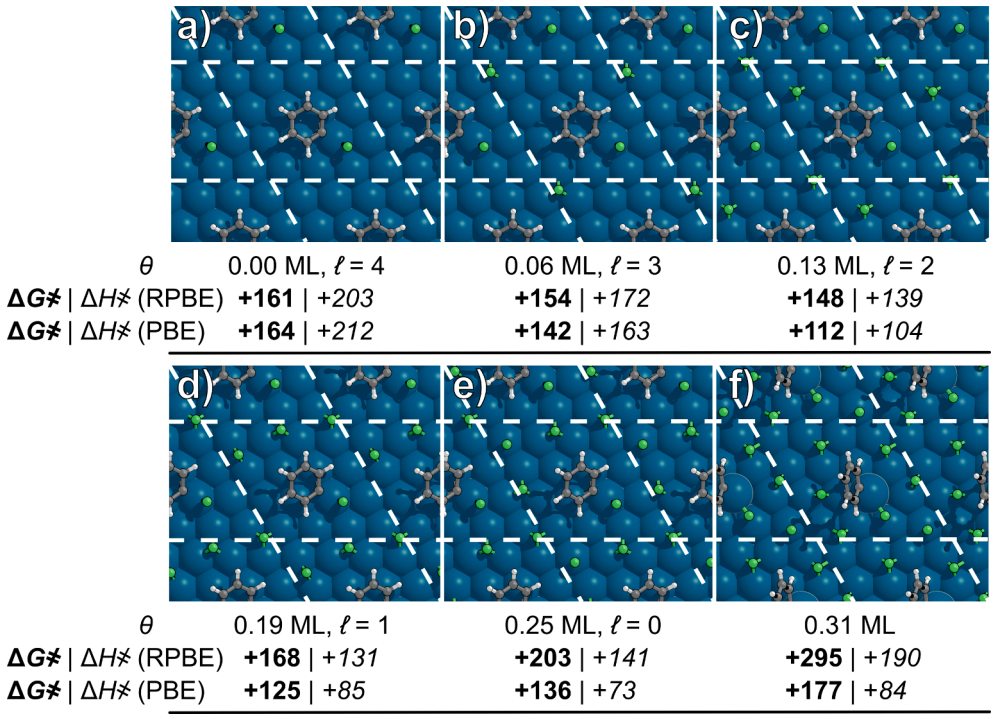

Fig. 6. Predicted transition state structures for C−Cl activation, the rate-determining step in PhCl hydrogenolysis. Image e) corresponds to $\ell = 0$, since 4Cl* on the surface is the reference state in this work. Cl* coverage increases from image a) to image f). Free energy and enthalpy barriers are in kJ mol^{-1}. The unit cell is denoted by dashed lines.

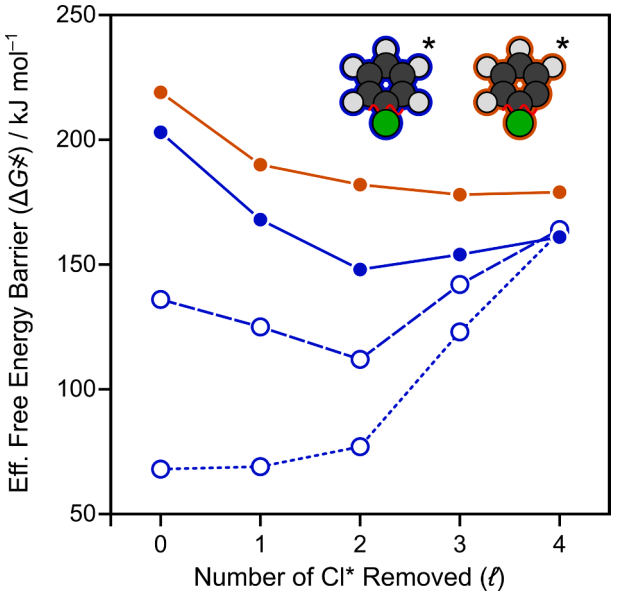

Fig. 7. Free energy barriers (ΔG≠; Eq. (9)) of C−Cl bond activation for PhCl* (blue) and ortho-C_6H_4Cl* (orange) as a function of Cl* removed from the surface before bond activation on a 4 × 4 Pd(1 1 1) surface model with 4Cl* (353 K, 1 bar H_2). Solid points were calculated with the RPBE functional, whereas hollow points were calculated with PBE (dashed line) and RPBE-D3 (dotted line). Enthalpy barriers (ΔH≠; Eq. (7)) and tabulated data are shown in the Supporting Information (Fig. S6, Table S6; SI).

hydrogenation of C_6H_5* to form benzene.

Reaction coordinate diagrams ($\Delta G^{\neq}$, 353 K) with (RPBE-D3) and without (RPBE) dispersion for Cl* reduction and desorption (as HCl), C–Cl activation, C–H formation, and desorption of produced benzene are shown in Fig. 8. Discussion centers around values without dispersion (RPBE) unless otherwise noted. In the mechanism consistent with the experimental kinetic trends, corresponding to $\ell = 1$, desorption of a single Cl* ($\Delta G = -1$ kJ mol^{-1}; Steps 1.1 and 1.2 combined) produces one HCl molecule. The relative free energies of the resulting states are near zero, consistent with Fig. 4 showing weak (near-zero) Cl* adsorption free energies near 0.25 ML. Surface Cl* desorptions are followed by adsorption of PhCl to form PhCl* (Step 1.3), which occurs with a large positive ΔG_{ads} (104 kJ mol^{-1}) when using RPBE, and with a negative ΔG_{ads} (−34 kJ mol^{-1}) when using RPBE-D3. This ~130 kJ mol^{-1} shift in adsorption free energy with dispersive interactions is likely an overestimate, but the large and positive values of ΔG_{ads} in the absence of dispersive corrections highlights the significant dipole–dipole interactions that are expected between large reactants and the catalyst surface.[86–93] Then C−Cl bond rupture occurs ($\Delta G^{\neq} = 168$ kJ mol^{-1}, $\Delta G_{act} = 65$ kJ mol^{-1}; Step 1.4), resulting in an adsorbed phenyl and Cl*. H_2 dissociatively adsorbs to the surface to provide an adsorbed H* ($\Delta G_{ads} = -1$ kJ mol^{-1}; Step 1.1), followed by hydrogenation of C_6H_5* ($\Delta G^{\neq} = 141$ kJ mol^{-1}, $\Delta G_{act} = 24$ kJ mol^{-1}; Step 1.5). The resulting adsorbed benzene ($\Delta G = 25$ kJ mol^{-1}; Step 1.6) then desorbs from the surface to regenerate the reference surface with 4Cl* ($\Delta G = -65$ kJ mol^{-1}; Step 1.6). In this sequence, the largest effective and intrinsic barriers occur for dechlorination ($\Delta G^{\neq} = 148$ kJ mol^{-1}, $\Delta G_{act} = 71$ kJ mol^{-1}; Step 1.4), regardless of whether RPBE or RPBE-D3 methods are used, suggesting it is indeed the sole rate-determining step, which is also consistent with our experimental kinetic isotope effect measurements.

The inconsistency between the DFT-predicted ℓ values (RPBE and PBE) and those from kinetic measurements could be explained by the lack of dispersive interactions (as suggested by the RPBE-D3 results) or from the shortcomings of flat, periodic surface models.[21,84,94,95] When transition states are larger than the species they replace during a kinetic cycle (in this case, the Ph−Cl*≠ is larger than the single Cl* it replaces), it creates strain in the adlayer for reactions at high coverage.[21] This strain, in the case of a flat periodic catalyst model, creates repulsive interactions between transition states in neighboring unit cells which consequently overestimates co-adsorbate interactions and

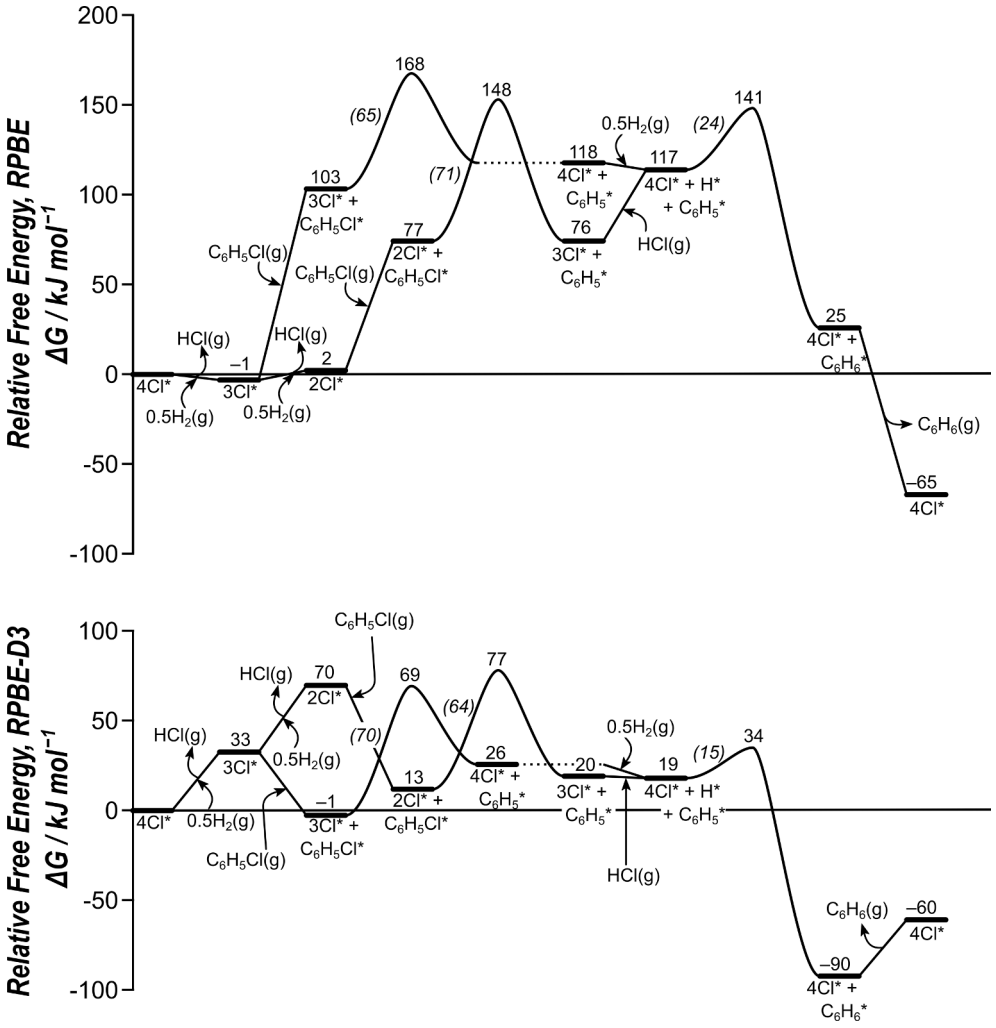

Fig. 8. DFT-derived reaction free energy diagram for two possible PhCl hydrogenolysis mechanisms calculated with RPBE ($\ell = 1$, $\Delta G^{\neq} = 168$ kJ mol^{-1}; $\ell = 2$, $\Delta G^{\neq} = 148$ kJ mol^{-1}) and RPBE-D3 ($\ell = 1$, $\Delta G^{\neq} = 69$ kJ mol^{-1}; $\ell = 2$, $\Delta G^{\neq} = 77$ kJ mol^{-1}) relative to a Pd(1 1 1) surface with 4Cl* and gas phase reactants at 353 K. Intrinsic activation barriers (ΔG_{act}) are provided in parentheses for each transition state and arrows indicate gaseous species adsorbing or desorbing from the catalyst surface.

overpredicts the desorption requirements from the adlayer. For example, calculations of ethane hydrogenolysis on similar flat periodic models predict that 4H* must desorb from a H*-covered Ir surface, in contrast to the 2H* predicted by calculations on a H*-covered Ir nanoparticle model (the latter of which being consistent with measured kinetic data).[19–21] Either of these explanations (overpredicted Cl* coverage or overpredicted co-adsorbate repulsions) would explain the slight inconsistency here with kinetic measurements. Overall, these DFT calculations help to explain the 'single-site' dechlorination observed by showing that both H* and C_6H_5* co-adsorbates can bind to the Pd surface within the Cl* adlayer without concomitant Cl* desorption, such that one Cl* is removed from the surface prior to dechlorination (which replaces that Cl*).

All DFT methods employed here suggest that Cl* surfaces saturate at coverages far beneath 1 ML, leaving interstitial sites that can bind H*, PhCl*, and the Ph* product of Ph−Cl dissociation. DFT-calculated adsorption energies for these species on Cl*-covered surfaces (0.25 ML) suggest that their adsorptions do not require concomitant Cl* desorption. In other words, our calculations suggest that the interstitial regions between Cl* can accommodate small amounts of these other reaction intermediates, consistent with Scheme 1. H* adsorption energies (referenced to ½ H_2) decrease from −38 kJ mol^{-1} on a bare Pd surface to −20 kJ mol^{-1} (or −29 kJ mol^{-1} with RPBE-D3) at 0.25 ML Cl* (Table S2), an increase consistent with co-adsorbate repulsions that are present, but ultimately too weak to prevent H* adsorption to such sites. PhCl* adsorption, similarly, is weakened by co-adsorbed Cl*, but its adsorption energy to interstitial sites is still −97 kJ mol^{-1} using RPBE-D3 (Table S3), suggesting that PhCl* can adsorb without requiring concomitant desorption of Cl*. These adsorption energies (Tables S2-S3), the activation free energies (Fig. 7-8), and the Ph−Cl*≠ transition state structures (Fig. 6) all suggest that incomplete coverage of Cl* on these metal surfaces enables this reaction, which forms two surface species (Ph* and Cl*), to occur following a single Cl* desorption (rather than two), consistent with the observed rate equation (Eq. (11). This can be conceptualized using a model characterized by two unique types of adsorption sites, in which one site-type (site 'a' in Scheme 1) reflects the Cl*-adlayer (saturated near 0.25–0.33 ML at conditions of interest) and the other site-type (site 'b' in Scheme 1) reflects interstitial regions within the Cl* adlayer that can bind PhCl*, H*, and Ph* intermediates necessary for PhCl hydrogenolysis.

4. Conclusions

Gas-phase kinetics for PhCl hydrodechlorination in a reaction-limited regime exhibit high selectivity (>95 %) for benzene production and HCl on 5 % Pd/C catalyst particles. Measured reaction orders are 1, 0.5, and −1 for PhCl, H_2, and HCl, respectively, consistent with previous work on PhCl hydrodechlorination.[47,48] Kinetic isotope

experiments found that hydrogen was not involved in the rate-determining step. As temperature is decreased, PhCl pressure dependence approaches zero, and H_2 pressure dependence remains nonzero, indicating competition between PhCl and H_2 adsorption. The MASI on the surface is most likely Cl* at conditions used in this study (99.6–101 kPa H_2, 0.2–1.1 kPa PhCl, 50 % PhCl conversion at 313 K, 323 K, 343 K, and 353 K).

A reaction mechanism was proposed based on insights from both kinetic experiments and theory. The mechanism assumes quasi-equilibrated adsorption and desorption events and kinetically relevant dechlorination as the sole rate-determining step. Experimental and DFT data agreed that no dehydrogenation of the phenyl ring occurs prior to the dechlorination, which can be attributed to the stability of an aromatic and the already unsaturated nature of the carbon involved in bond cleavage. This contrasts with the reactive intermediates predicted for saturated species, as the carbon on methyl chloride is predicted to undergo two dehydrogenation events.[27] DFT results suggest that H* and C_6H_5* species are not in site competition with Cl* (depicted here as a two-site mechanism) because those species bind interstitially within the Cl* adlayer without requiring Cl* desorption to occur. This is because Cl* coverages are far less than unity and Cl* species are mobile. Cl* coverages do not reach a 1:1 Cl*:Pd_{surf} saturation, and likely saturate closer to 1:3 or even 1:4 Cl*:Pd_{surf} at these conditions (313–353 K, H_2/HCl near 100). Cl* diffusion barriers on Pd(1 1 1) are <10 kJ mol^{-1}. These data can be described using a two-site mechanism that requires one Cl* desorption prior to dechlorination and leads to a rate equation in agreement with kinetic data measured here and in prior work[35,47,48] with a more-physical underpinning than the single-site Eley-Rideal style mechanism previously accepted.[47]

Credit authorship contribution statement

Nikki Kragt: Writing – review & editing, Writing – original draft, Methodology, Investigation, Conceptualization. **Jalal Tavana:** Data curation, Writing – original draft, Investigation, Formal analysis. **Mohammed Al-Gharrawi:** Data curation, Investigation. **M. Clayton Wheeler:** Conceptualization, Supervision. **David Hibbitts:** Writing – review & editing, Writing – original draft, Supervision, Project administration, Funding acquisition, Conceptualization. **Thomas J. Schwartz:** Writing – review & editing, Writing – original draft, Supervision, Project administration, Methodology, Funding acquisition, Conceptualization.

Declaration of competing interest

The authors declare that they have no known competing financial interests or personal relationships that could have appeared to influence the work reported in this paper.

Data availability

Data will be made available on request.

Acknowledgements

The work at UMaine was supported in part by the donors of the ACS Petroleum Research Fund under Doctoral New Investigator Grant 56712-DNI5. T.J.S. served as Principal Investigator on ACS PRF 56712-DNI5 that provided support for J.T. This work was also supported in part by the University of Maine Office of the Vice President for Research. The work at UF was financially supported by the Moreno Rising Star Professorship. This work used the Bridges cluster at the University of Pittsburgh through allocation cts200023p from the Advanced Cyberinfrastructure Coordination Ecosystem: Services & Support (ACCESS) program, which is supported by National Science Foundation grants #2138259, #2138286, #2138307, #2137603, and #2138296. We acknowledge Nathan Hill for assistance with equipment construction and Profs. Brian G. Frederick, Lars Grabow, and Rachel N. Austin for helpful discussions.

Appendix A. Supplementary data

Supplementary data to this article can be found online at https://doi.org/10.1016/j.jcat.2024.115435.

References

[1] X. Wei, X. Wan, Z. Sun, J. Miao, R. Zhang, Q.J. Niu, Understanding Electrocatalytic Hydrodechlorination of Chlorophenols on Palladium-Modified Cathode in Aqueous Solution, ACS Omega 3 (2018) 5876–5886, https://doi.org/10.1021/acsomega.8b00624.
[2] Z. Peng, X. Wang, Z. Li, X. Chen, Y. Ding, J. Zhang, Liquid-phase catalytic hydrodechlorination of chlorinated organic compounds in a continuous flow micro-packed bed reactor over a Pd/AC catalyst, React, Chem. Eng. 7 (2022) 1827–1835, https://doi.org/10.1039/D2RE00043A.
[3] J. Chen, S. Zhou, X. Liu, J. Zhang, Gas-phase Hydrodechlorination of Chlorobenzene Over Silica-supported Ni2P Catalysts Prepared Under Different Reduction Conditions, Catal. Lett. 122 (2008) 167–175, https://doi.org/10.1007/s10562-007-9363-7.
[4] E.S. Lokteva, V.V. Shishova, N.N. Tolkachev, A.N. Kharlanov, K.I. Maslakov, A. O. Kamaev, I.Y. Kaplin, I.N. Savina, E.V. Golubina, Hydrodechlorination of 4-Chlorophenol on Pd-Fe Catalysts on Mesoporous ZrO2SiO2 Support, Molecules 26 (2020) 1–25, https://doi.org/10.3390/molecules26010141.
[5] J.A. Cecilia, A. Infantes-Molina, E. Rodríguez-Castellón, A. Jiménez-López, Gas phase catalytic hydrodechlorination of chlorobenzene over cobalt phosphide catalysts with different P contents, J. Hazard. Mater. 260 (2013) 167–175, https://doi.org/10.1016/j.jhazmat.2013.05.013.
[6] B. Okolo, C. Park, M.A. Keane, Interaction of Phenol and Chlorophenols with Activated Carbon and Synthetic Zeolites in Aqueous Media, J. Colloid Interface Sci. 226 (2000) 308–317, https://doi.org/10.1006/jcis.2000.6796.
[7] G.R. Lester, Catalytic destruction of hazardous halogenated organic chemicals, Catal. Today. 53 (1999) 407–418, https://doi.org/10.1016/S0920-5861(99)00134-0.
[8] D.R. van der Vaart, E.G. Marchand, A. Bagely-Pride, Thermal and catalytic incineration of volatile organic compounds, Crit. Rev. Environ. Sci. Technol. 24 (1994) 203–236, https://doi.org/10.1080/10643389409388466.
[9] Y. Hashimoto, Y. Uemichi, A. Ayame, Low-temperature hydrodechlorination mechanism of chlorobenzenes over platinum-supported and palladium-supported alumina catalysts, Appl. Catal. A. 287 (2005) 89–97, https://doi.org/10.1016/j.apcata.2005.03.039.
[10] M.A. Keane, Hydrodehalogenation of haloarenes over Silica supported Pd and Ni, Appl. Catal. A. 271 (2004) 109–118, https://doi.org/10.1016/j.apcata.2004.02.051.
[11] E. Piera, J.C. Calpe, E. Brillas, X. Domènech, J. Peral, 2,4-Dichlorophenoxyacetic acid degradation by catalyzed ozonation: TiO2/UVA/O3 and Fe(II)/UVA/O3 systems, Appl. Catal. b. 27 (2000) 169–177, https://doi.org/10.1016/S0926-3373(00)00149-1.
[12] C.S. Fang, S.-L. Khor, Reduction of volatile organic compounds in aqueous solutions through air stripping and gas-phase carbon adsorption, Environ. Prog. 8 (1989) 270–278, https://doi.org/10.1002/ep.3300080422.
[13] J. Luis Benítez A., G.D. Angel, Total hydrodechlorination of industrial transformer oil on metal-supported catalysts Chem. Eng. Commun. 196 (2009) 1217 1226 10.1080/00986440902831888.
[14] V.I. Simagina, E.S. Tayban, E.D. Grayfer, A.G. Gentsler, O.V. Komova, O. V. Netskina, Liquid-phase hydrodechlorination of chlorobenzene by molecular hydrogen: the influence of reaction medium on process efficiency, Pure Appl. Chem. 81 (2009) 2107–2114, https://doi.org/10.1351/PAC-CON-08-10-12.
[15] E.V. Golubina, T.N. Rostovshchikova, E.S. Lokteva, K.I. Maslakov, S.A. Nikolaev, T. B. Egorova, S.A. Gurevich, V.M. Kozhevin, D.A. Yavsin, A. Ye, Yermakov, Chlorobenzene hydrodechlorination on bimetallic catalysts prepared by laser electrodispersion of NiPd alloy, Pure Appl. Chem. 90 (2018) 1685–1701, https://doi.org/10.1515/pac-2018-0207.
[16] C. Amorim, G. Yuan, P. Patterson, M. Keane, Catalytic hydrodechlorination over Pd supported on amorphous and structured carbon, J. Catal. 234 (2005) 268–281, https://doi.org/10.1016/j.jcat.2005.06.019.
[17] Z.C. Zhang, B.C. Beard, Genesis of durable catalyst for selective hydrodechlorination of CCl4 to CHCl3, Appl. Catal. A 174 (1998) 33–39, https://doi.org/10.1016/S0926-860X(98)00150-1.
[18] J.H. Sinfelt, Catalytic hydrogenolysis on metals, Catal. Lett. 9 (1991) 159–171, https://doi.org/10.1007/BF00773174.
[19] A. Almithn, D. Hibbitts, Comparing Rate and Mechanism of Ethane Hydrogenolysis on Transition-Metal Catalysts, J. Phys. Chem. c. 123 (2019) 5421–5432, https://doi.org/10.1021/acs.jpcc.8b11070.
[20] D.W. Flaherty, D.D. Hibbitts, E.I. Gürbüz, E. Iglesia, Theoretical and kinetic assessment of the mechanism of ethane hydrogenolysis on metal surfaces saturated with chemisorbed hydrogen, J. Catal. 311 (2014) 350–356, https://doi.org/10.1016/j.jcat.2013.11.026.
[21] A. Almithn, D. Hibbitts, Effects of catalyst model and high adsorbate coverages in ab initio studies of alkane hydrogenolysis, ACS Catal. 8 (2018) 6375–6387, https://doi.org/10.1021/acscatal.8b01114.

[22] D.W. Flaherty, E. Iglesia, Transition-state enthalpy and entropy effects on reactivity and selectivity in hydrogenolysis of n-alkanes, J. Am. Chem. Soc. 135 (2013) 18586–18599, https://doi.org/10.1021/ja4093743.

[23] D.D. Hibbitts, D.W. Flaherty, E. Iglesia, Effects of chain length on the mechanism and rates of metal-catalyzed hydrogenolysis of n-alkanes, J. Phys. Chem. c. 120 (2016) 8125–8138, https://doi.org/10.1021/acs.jpcc.6b00323.

[24] G. Zichittella, A.M. Ebrahim, J. Zhu, A.E. Brenner, G. Drake, G.T. Beckham, S. R. Bare, J.E. Rorrer, Y. Román-Leshkov, Hydrogenolysis of Polyethylene and Polypropylene into Propane over Cobalt-Based Catalysts, JACS Au. 2 (2022) 2259–2268, https://doi.org/10.1021/jacsau.2c00402.

[25] P.A. Kots, T. Xie, B.C. Vance, C.M. Quinn, M.D. de Mello, J.A. Boscoboinik, C. Wang, P. Kumar, E.A. Stach, N.S. Marinkovic, L. Ma, S.N. Ehrlich, D.G. Vlachos, Electronic modulation of metal-support interactions improves polypropylene hydrogenolysis over ruthenium catalysts, Nat. Commun. 13 (2022) 5186, https://doi.org/10.1038/s41467-022-32934-5.

[26] J. Shangguan M.V. Olarte Y.-H. (Cathy) Chin, Mechanistic insights on C-O and C-C bond activation and hydrogen insertion during acetic acid hydrogenation catalyzed by ruthenium clusters in aqueous medium J. Catal. 340 2016 107 121 10.1016/j.jcat.2016.04.024.

[27] A.S. Almithn, D.D. Hibbitts, Impact of metal and heteroatom identities in the hydrogenolysis of C-X bonds (X = C, N, O, S, and cl), ACS Catal. 10 (2020) 5086–5100, https://doi.org/10.1021/acscatal.0c00481.

[28] E.I. Gürbüz, D.D. Hibbitts, E. Iglesia, Kinetic and mechanistic assessment of alkanol/alkanal decarbonylation and deoxygenation pathways on metal catalysts, J. Am. Chem. Soc. 137 (2015) 11984–11995, https://doi.org/10.1021/jacs.5b05361.

[29] D.D. Hibbitts, D.W. Flaherty, E. Iglesia, Role of branching on the rate and mechanism of C-C cleavage in alkanes on metal surfaces, ACS Catal. 6 (2016) 469–482, https://doi.org/10.1021/acscatal.5b01950.

[30] D.W. Flaherty, D.D. Hibbitts, E. Iglesia, Metal-catalyzed C-C bond cleavage in alkanes: effects of methyl substitution on transition-state structures and stability, J. Am. Chem. Soc. 136 (2014) 9664–9676, https://doi.org/10.1021/ja5037429.

[31] C. Jia, S. Xie, W. Zhang, N.N. Intan, J. Sampath, J. Pfaendtner, H. Lin, Deconstruction of high-density polyethylene into liquid hydrocarbon fuels and lubricants by hydrogenolysis over Ru catalyst, Chem, Catalysis. 1 (2021) 437–455, https://doi.org/10.1016/j.checat.2021.04.002.

[32] D.W. Flaherty, A. Uzun, E. Iglesia, Catalytic ring opening of cycloalkanes on ir clusters: alkyl substitution effects on the structure and stability of C-C bond cleavage transition states, J. Phys. Chem. c. 119 (2015) 2597–2613, https://doi.org/10.1021/jp511688x.

[33] T. Patra, S. Agasti, A. Modak, D. Maiti, Nickel-catalyzed hydrogenolysis of unactivated carbon-cyano bonds, Chem. Commun. 49 (2013) 8362–8364, https://doi.org/10.1039/c3cc44562c.

[34] C. Zhao, J.A. Lercher, Catalytic depolymerization and deoxygenation of lignin, in: The Role of Catalysis for the Sustainable Production of Bio-Fuels and Bio-Chemicals, Elsevier, 2013: pp. 289-320. https://doi.org/10.1016/B978-0-444-56330-9.00009-7.

[35] C.D. Thompson, R.M. Rioux, N. Chen, F.H. Ribeiro, Turnover rate, reaction order, and elementary steps for the hydrodechlorination of chlorofluorocarbon compounds on palladium catalysts, J. Phys. Chem. b. 104 (2000) 3067–3077, https://doi.org/10.1021/jp992888n.

[36] E. Diaz, A.F. Mohedano, J.A. Casas, C. Shalaby, S. Eser, J.J. Rodriguez, On the performance of Pd and Rh catalysts over different supports in the hydrodechlorination of the MCPA herbicide, Appl. Catal. b. 186 (2016) 151–156, https://doi.org/10.1016/j.apcatb.2015.12.054.

[37] S.V. Klokov, E.S. Lokteva, E.V. Golubina, K.I. Maslakov, A.V. Levanov, S. A. Chernyak, V.A. Likholobov, Effective Pd/C catalyst for chlorobenzene and hexachlorobenzene hydrodechlorination by direct pyrolysis of sawdust impregnated with palladium nitrate, Catal. Commun. 77 (2016) 37–41, https://doi.org/10.1016/j.catcom.2016.01.013.

[38] E.N. Balko, E. Przybylski, F. Von Trentini, Exhaustive liquid-phase catalytic hydrodehalogenation of chlorobenzenes, Appl. Catal. b. 2 (1993) 1–8, https://doi.org/10.1016/0926-3373(93)80023-7.

[39] R. Gopinath, N. Lingaiah, N. Seshu Babu, I. Suryanarayana, P.S. Sai Prasad, A. Obuchi, A highly active low Pd content catalyst synthesized by deposition-precipitation method for hydrodechlorination of chlorobenzene, J. Mol. Catal. a: Chem. 223 (2004) 289–293, https://doi.org/10.1016/j.molcata.2003.09.046.

[40] C. Park, C. Menini, J.L. Valverde, M.A. Keane, Carbon-chlorine and carbon-bromine bond cleavage in the catalytic hydrodehalogenation of halogenated aromatics, J. Catal. 211 (2002) 451–463, https://doi.org/10.1006/jcat.2002.3750.

[41] C.-J. Chen, W.-S. Lee, A. Bhan, Mo2C catalyzed vapor phase hydrodeoxygenation of lignin-derived phenolic compound mixtures to aromatics under ambient pressure, Appl. Catal. A 510 (2016) 42–48, https://doi.org/10.1016/j.apcata.2015.10.043.

[42] M. Wang, H. Shi, D.M. Camaioni, J.A. Lercher, Palladium-Catalyzed Hydrolytic Cleavage of Aromatic C-O Bonds, Angew. Chem. Int. Ed. 56 (2017) 2110–2114, https://doi.org/10.1002/anie.201611076.

[43] Q. Bu, H. Lei, A.H. Zacher, L. Wang, S. Ren, J. Liang, Y. Wei, Y. Liu, J. Tang, Q. Zhang, R. Ruan, A review of catalytic hydrodeoxygenation of lignin-derived phenols from biomass pyrolysis, Bioresour. Technol. 124 (2012) 470–477, https://doi.org/10.1016/j.biortech.2012.08.089.

[44] K.H. Kim, K. Jeong, J. Zhuang, H.J. Jeong, C.S. Kim, B. Koo, C.G. Yoo, Tandem conversion of lignin to catechols via demethylation and catalytic hydrogenolysis, Ind. Crop. Prod. 159 (2021) 113095, https://doi.org/10.1016/j.indcrop.2020.113095.

[45] Y. Cai, W. Liu, Y. Yu, L. Liu, Q. Pei, H. Wu, T. He, J. Guo, A. Wu, P. Chen, Transition Metal-Free Hydrogenolysis of Anilines to Arenes Mediated by Lithium Hydride, J. Am. Chem. Soc. 144 (2022) 17441–17448, https://doi.org/10.1021/jacs.2c05586.

[46] L. Prati, Reductive catalytic dehalogenation of light chlorocarbons, Appl. Catal. b. 23 (1999) 135–142, https://doi.org/10.1016/S0926-3373(99)00071-5.

[47] B. Coq, Conversion of chlorobenzene over palladium and rhodium catalysts of widely varying dispersion, J. Catal. 101 (1986) 434–445, https://doi.org/10.1016/0021-9517(86)90271-X.

[48] K. Konuma, N. Kameda, Effect of substituents on the hydrodechlorination reactivity of para-substituted chlorobenzenes, J. Mol. Catal. a: Chem. 178 (2002) 239–251, https://doi.org/10.1016/S1381-1169(01)00337-5.

[49] P. Gelin, A.R. Siedle, J.T. Yates, Stoichiometric adsorbate species interconversion processes in the chemisorbed layer. An infrared study of the carbon monoxide/palladium system, J. Phys. Chem. 88 (1984) 2978–2985, https://doi.org/10.1021/j150658a012.

[50] G. Bergeret, P. Gallezot, Particle size and dispersion measurements, in: G. Ertl, H. Knözinger, F. Schüth, J. Weitkamp (Eds.), Handbook of Heterogeneous Catalysis: Online, Wiley-VCH Verlag GmbH & Co. KGaA, Weinheim, Germany, 2008, https://doi.org/10.1002/9783527610044.hetcat0038.

[51] V.W. Weekman, Laboratory reactors and their limitations, AIChE J. 20 (1974) 833–840, https://doi.org/10.1002/aic.690200502.

[52] G. Kresse, J. Furthmüller, Efficiency of ab-initio total energy calculations for metals and semiconductors using a plane-wave basis set, Comp. Mater. Sci. 6 (1996) 15–50, https://doi.org/10.1016/0927-0256(96)00008-0.

[53] G. Kresse, J. Furthmüller, Efficient iterative schemes for *ab initio* total-energy calculations using a plane-wave basis set, Phys. Rev. b. 54 (1996) 11169–11186, https://doi.org/10.1103/PhysRevB.54.11169.

[54] G. Kresse, J. Hafner, *Ab initio* molecular dynamics for liquid metals, Phys. Rev. b. 47 (1993) 558–561, https://doi.org/10.1103/PhysRevB.47.558.

[55] G. Kresse, J. Hafner, *Ab initio* molecular-dynamics simulation of the liquid-metal-amorphous-semiconductor transition in germanium, Phys. Rev. b. 49 (1994) 14251–14269, https://doi.org/10.1103/PhysRevB.49.14251.

[56] J. Hafner, Ab-initio simulations of materials using VASP: density-functional theory and beyond, J. Comput. Chem. 29 (2008) 2044–2078, https://doi.org/10.1002/jcc.21057.

[57] P. Kravchenko, C. Plaisance, D. Hibbitts, A new computational interface for catalysis, Published as pre-print on https://chemrxiv.org/articles/preprint/8040737 (2019). https://doi.org/10.26434/chemrxiv.8040737.v3.

[58] B. Hammer, L.B. Hansen, J.K. Nørskov, Improved adsorption energetics within density-functional theory using revised Perdew-Burke-Ernzerhof functionals, Phys. Rev. b. 59 (1999) 7413–7421, https://doi.org/10.1103/PhysRevB.59.7413.

[59] J.P. Perdew, K. Burke, M. Ernzerhof, Generalized gradient approximation made simple, Phys. Rev. Lett. 77 (1996) 3865–3868, https://doi.org/10.1103/PhysRevLett.77.3865.

[60] Y. Zhang, W. Yang, Comment on "Generalized Gradient Approximation Made Simple", Phys. Rev. Lett. 80 (1998) 890, https://doi.org/10.1103/PhysRevLett.80.890.

[61] S. Grimme, J. Antony, S. Ehrlich, H. Krieg, A consistent and accurate ab initio parametrization of density functional dispersion correction (DFT-D) for the 94 elements H-Pu, J. Chem. Phys. 132 (2010) 154104, https://doi.org/10.1063/1.3382344.

[62] S. Grimme, S. Ehrlich, L. Goerigk, Effect of the damping function in dispersion corrected density functional theory, J. Comput. Chem. 32 (2011) 1456–1465, https://doi.org/10.1002/jcc.21759.

[63] P.E. Blöchl, Projector augmented-wave method, Phys. Rev. b. 50 (1994) 17953–17979, https://doi.org/10.1103/PhysRevB.50.17953.

[64] G. Kresse, D. Joubert, From ultrasoft pseudopotentials to the projector augmented-wave method, Phys. Rev. b. 59 (1999) 1758–1775, https://doi.org/10.1103/PhysRevB.59.1758.

[65] H.J. Monkhorst, J.D. Pack, Special points for Brillouin-zone integrations, Phys. Rev. b. 13 (1976) 5188–5192, https://doi.org/10.1103/PhysRevB.13.5188.

[66] J.D. Pack, H.J. Monkhorst, Special points for Brillouin-zone integrations—a reply, Phys. Rev. b. 16 (1977) 1748–1749, https://doi.org/10.1103/PhysRevB.16.1748.

[67] G. Henkelman, H. Jónsson, Improved tangent estimate in the nudged elastic band method for finding minimum energy paths and saddle points, J. Chem. Phys. 113 (2000) 9978–9985, https://doi.org/10.1063/1.1323224.

[68] H. Jónsson, G. Mills, K.W. Jacobsen, Nudged elastic band method for finding minimum energy paths of transitions, in: B.J. Berne, G. Ciccotti, D.F. Coker (Eds.), Classical and Quantum Dynamics in Condensed Phase Simulations, World Scientific, 1998, pp. 385–404, https://doi.org/10.1142/9789812839664_0016.

[69] G. Henkelman, H. Jónsson, A dimer method for finding saddle points on high dimensional potential surfaces using only first derivatives, J. Chem. Phys. 111 (1999) 7010–7022, https://doi.org/10.1063/1.480097.

[70] S.H. Krishna, R.S. Assary, Q.A. Rashke, Z.R. Schmidt, L.A. Curtiss, J.A. Dumesic, G. W. Huber, Mechanistic Insights into the Hydrogenolysis of Levoglucosanol over Bifunctional Platinum Silica-Alumina Catalysts, ACS Catal. 8 (2018) 3743–3753, https://doi.org/10.1021/acscatal.7b03764.

[71] M.E. Witzke, A. Almithn, C.L. Coonrod, M.D. Triezenberg, D.D. Hibbitts, D. W. Flaherty, In Situ Methods for Identifying Reactive Surface Intermediates during Hydrogenolysis Reactions: C-O Bond Cleavage on Nanoparticles of Nickel and Nickel Phosphides, J. Am. Chem. Soc. 141 (2019) 16671–16684, https://doi.org/10.1021/jacs.9b06112.

[72] J.R. Engstrom, D.W. Goodman, W.H. Weinberg, Hydrogenolysis of ethane, propane, n-butane, and neopentane on the (111) and (110)-(1×2) surfaces of

iridium, J. Am. Chem. Soc. 110 (1988) 8305–8319, https://doi.org/10.1021/ja00233a005.
[73] P.B. Weisz, C.D. Prater, Interpretation of measurements in experimental catalysis, in, Elsevier (1954) 143–196, https://doi.org/10.1016/S0360-0564(08)60390-9.
[74] O. Levenspiel, Chemical Reaction Engineering, 3rd Edition, 3rd ed., Wiley, New York, 1998.
[75] J. Lu, S. Behtash, M. Faheem, A. Heyden, Microkinetic modeling of the decarboxylation and decarbonylation of propanoic acid over Pd(111) model surfaces based on parameters obtained from first principles, J. Catal. 305 (2013) 56–66, https://doi.org/10.1016/j.jcat.2013.04.026.
[76] W. Yang, R.V. Solomon, O. Mamun, J.Q. Bond, A. Heyden, Investigation of the reaction mechanism of the hydrodeoxygenation of propionic acid over a Rh(1 1 1) surface: a first principles study, J. Catal. 391 (2020) 98–110, https://doi.org/10.1016/j.jcat.2020.08.015.
[77] E. Yik, D. Hibbitts, H. Wang, E. Iglesia, Hydrogenation and C-S bond activation pathways in thiophene and tetrahydrothiophene reactions on sulfur-passivated surfaces of Ru, Pt, and Re nanoparticles, Appl. Catal. b. 291 (2021) 119797, https://doi.org/10.1016/j.apcatb.2020.119797.
[78] C.T. Campbell, J.R.V. Sellers, The entropies of adsorbed molecules, J. Am. Chem. Soc. 134 (2012) 18109–18115, https://doi.org/10.1021/ja3080117.
[79] C.T. Campbell, J.R.V. Sellers, Correction to “the entropies of adsorbed molecules”, J. Am. Chem. Soc. 135 (2013) 13998, https://doi.org/10.1021/ja407293b.
[80] A. Bajpai, P. Mehta, K. Frey, A.M. Lehmer, W.F. Schneider, Benchmark First-Principles Calculations of Adsorbate Free Energies, ACS Catal. 8 (2018) 1945–1954, https://doi.org/10.1021/acscatal.7b03438.
[81] C. Waitt, A.R. Miles, W.F. Schneider, Adsorbate Free Energies from DFT-Derived Translational Energy Landscapes, J. Phys. Chem. c. 125 (2021) 20331–20342, https://doi.org/10.1021/acs.jpcc.1c05917.
[82] M. García-Diéguez, D.D. Hibbitts, E. Iglesia, Hydrogen chemisorption isotherms on platinum particles at catalytic temperatures: langmuir and two-dimensional gas models revisited, J. Phys. Chem. c. 123 (2019) 8447–8462, https://doi.org/10.1021/acs.jpcc.8b10877.
[83] K. Yang, J. Zheng, Y. Zhao, D.G. Truhlar, Tests of the RPBE, revPBE, tau-HCTHhyb, omegaB97X-D, and MOHLYP density functional approximations and 29 others against representative databases for diverse bond energies and barrier heights in catalysis, J. Chem. Phys. 132 (2010) 164117, https://doi.org/10.1063/1.3382342.
[84] D.D. Hibbitts, E. Dybeck, T. Lawlor, M. Neurock, E. Iglesia, Preferential activation of CO near hydrocarbon chains during Fischer-Tropsch synthesis on Ru, J. Catal. 337 (2016) 91–101, https://doi.org/10.1016/j.jcat.2016.01.010.
[85] W. Erley, Chlorine adsorption on the (111) faces of Pd and Pt, Surf. Sci. 94 (1980) 281–292, https://doi.org/10.1016/0039-6028(80)90007-2.
[86] S.J. Jenkins, Aromatic adsorption on metals via first-principles density functional theory, Proceedings of the Royal Society A: Mathematical, Physical and Engineering Sciences. 465 (2009) 2949-2976. https://doi.org/10.1098/rspa.2009.0119.
[87] K. Tonigold, A. Gross, Adsorption of small aromatic molecules on the (111) surfaces of noble metals: a density functional theory study with semiempirical corrections for dispersion effects, J. Chem. Phys. 132 (2010) 224701, https://doi.org/10.1063/1.3439691.
[88] O. Bauer, G. Mercurio, M. Willenbockel, W. Reckien, C. Heinrich Schmitz, B. Fiedler, S. Soubatch, T. Bredow, F.S. Tautz, M. Sokolowski, Role of functional groups in surface bonding of planar-conjugated molecules, Phys. Rev. b. 86 (2012) 235431, https://doi.org/10.1103/PhysRevB.86.235431.
[89] W. Liu, J. Carrasco, B. Santra, A. Michaelides, M. Scheffler, A. Tkatchenko, Benzene adsorbed on metals: concerted effect of covalency and van der Waals bonding, Phys. Rev. b. 86 (2012), https://doi.org/10.1103/PhysRevB.86.245405.
[90] W. Liu, V.G. Ruiz, G.-X. Zhang, B. Santra, X. Ren, M. Scheffler, A. Tkatchenko, Structure and energetics of benzene adsorbed on transition-metal surfaces: density-functional theory with van der Waals interactions including collective substrate response, New J. Phys. 15 (2013) 053046, https://doi.org/10.1088/1367-2630/15/5/053046.
[91] W. Reckien, M. Eggers, T. Bredow, Theoretical study of the adsorption of benzene on coinage metals, Beilstein J. Org. Chem. 10 (2014) 1775–1784, https://doi.org/10.3762/bjoc.10.185.
[92] W. Liu, S.N. Filimonov, J. Carrasco, A. Tkatchenko, Molecular switches from benzene derivatives adsorbed on metal surfaces, Nat. Commun. 4 (2013) 2569, https://doi.org/10.1038/ncomms3569.
[93] Y. Jiang, S. Yang, S. Li, W. Liu, Aromatic molecules on low-index coinage metal surfaces: Many-body dispersion effects, Sci. Rep. 6 (2016) 39529, https://doi.org/10.1038/srep39529.
[94] B.T. Loveless, C. Buda, M. Neurock, E. Iglesia, CO chemisorption and dissociation at high coverages during CO hydrogenation on Ru catalysts, J. Am. Chem. Soc. 135 (2013) 6107–6121, https://doi.org/10.1021/ja311848e.
[95] J. Liu, D. Hibbitts, E. Iglesia, Dense CO adlayers as enablers of CO hydrogenation turnovers on Ru surfaces, J. Am. Chem. Soc. 139 (2017) 11789–11802, https://doi.org/10.1021/jacs.7b04606.